

# Marcela Areyano<sup>1,2</sup>

Department of Mechanical Engineering, University of California, Santa Barbara, Santa Barbara, CA 93106 e-mail: m\_areyano@ucsb.edu

# Jamie A. Booth<sup>2</sup>

Mem. ASME Department of Mechanical Engineering, California State University, Northridge, Northridge, CA 91330 e-mail: jamie.booth@csun.edu

# Dane Brouwer<sup>3</sup>

Department of Mechanical Engineering, University of California, Santa Barbara, Santa Barbara, CA 93106 e-mail: daneb@stanford.edu

# Luke F. Gockowski

Department of Mechanical Engineering, University of California, Santa Barbara, Santa Barbara, CA 93106 e-mail: Igockowski@ucsb.edu

# Megan T. Valentine

Mem. ASME

Department of Mechanical Engineering, University of California, Santa Barbara, Santa Barbara, CA 93106 e-mail: valentine@engineering.ucsb.edu

# Robert M. McMeeking

Fellow ASME
Department of Mechanical Engineering,
University of California, Santa Barbara,
Santa Barbara, CA 93106;
Department of Materials,
University of California, Santa Barbara,
Santa Barbara, CA 93106;
School of Engineering,
University of Aberdeen,
Aberdeen AB24 3UE, UK;
INM—Leibniz Institute for New Materials,
Campus D2 2, Saarbrücken, Germany
e-mail: rmcm@ucsb.edu

# Suction-Controlled Detachment of Mushroom-Shaped Adhesive Structures

Experimental evidence suggests that suction may play a role in the attachment strength of mushroom-tipped adhesive structures, but the system parameters which control this effect are not well established. A fracture mechanics-based model is introduced to determine the critical stress for defect propagation at the interface in the presence of trapped air. These results are compared with an experimental investigation of millimeter-scale elastomeric structures. These structures are found to exhibit a greater increase in strength due to suction than is typical in the literature, as they have a large tip diameter relative to the stalk. The model additionally provides insight into differences in expected behavior across the design space of mushroom-shaped structures. For example, the model reveals that the suction contribution is length-scale dependent. It is enhanced for larger structures due to increased volume change, and thus the attainment of lower pressures, inside of the defect. This scaling effect is shown to be less pronounced if the tip is made wider relative to the stalk. An asymptotic result is also provided in the limit that the defect is far outside of the stalk, showing that the critical stress is lower by a factor of 1/2 than the result often used in the literature to estimate the effect of suction. This discrepancy arises as the latter considers only the balance of remote stress and pressure inside the defect and neglects the influence of compressive tractions outside of the defect. [DOI: 10.1115/1.4049392]

Keywords: energy release rate and delamination, mechanical properties of materials, structures

### 1 Introduction

Fibrillar adhesives inspired by nature have long been studied for their superb adhesive properties in both reversible and permanent adhesion. Attachment structures and sizes utilized in nature range from nanoscale spatula tips observed in geckos, to macroscale spatula plaques used to permanently adhere by marine mussels [1–3]. Although the source of adhesion is different in the two systems, with geckos relying on intermolecular van der Waals

forces [4] and marine mussels on chemical bonding [5], both of these systems appear to make use of mushroom-shaped geometries [5,6]. Studies of synthetic mushroom-shaped microstructures show improvements in the adhesion strength by factors as high as 30 times that of straight punches [7,8]. These improvements have led to the use of micropatterned surfaces in various applications, including climbing robots and in pick-and-place operations [9–11]. The high adhesion of these structures is the result of the mitigation of the severe stress concentration which occurs at the contact edge of a punch [7,12,13]. The inclusion of the thin flange at the tip has the effect of reducing strain energy at the contact edge and creating a turning action which results in a compressive contribution to the stresses in this region. This leads to a preference for defect propagation from the center of the contact [14,15]. Mitigation of the contact edge stress concentration in mushroom-shaped structures has inspired other designs which harness similar effects, including those based on combining multiple materials [16-19] or using cupped tip geometries [20,21].

<sup>&</sup>lt;sup>1</sup>Corresponding author.

<sup>&</sup>lt;sup>2</sup>Co-first authors

<sup>&</sup>lt;sup>3</sup>Present address: Department of Mechanical Engineering, Stanford University, Stanford, CA 94305.

Contributed by the Applied Mechanics Division of ASME for publication in the JOURNAL OF APPLIED MECHANICS. Manuscript received September 29, 2020; final manuscript received December 8, 2020; published online January 6, 2021. Assoc. Editor: Annie Ruimi.

One effect not given significant attention in the modeling of mushroom-tipped structures is the role of suction. Many groups have sought to investigate this effect experimentally by reducing the atmospheric pressure under which mechanical testing is performed, without clear consensus. Henrey et al. reported no dependence on ambient atmospheric pressure for an array of microstructures with 17  $\mu$ m tip diameter [22]. Likewise, Sameoto et al. reported little to no change in the pull-off force (defined as the maximum tensile load supported by the junction) with pressure for tip diameters of 16  $\mu$ m or less [23]. However, a significant number of other studies have shown that pull-off force is lowered in a reduced pressure environment [24-27]. Heepe et al. showed that for an array of  $50 \,\mu\mathrm{m}$  diameter mushroom-tipped structures, the absence of suction led to a 10% reduction in the pull-off force [24]. Crucially, the authors also highlighted that the suction contribution was dependent on the retraction velocity and suggested this was the result of imperfect sealing of the defect which allowed for equalization of the pressure difference over longer loading times. Tinnemann et al. tested mushroom-shaped structures with tip diameter of  $710 \, \mu \mathrm{m}$ under various atmospheric pressures, and on rough and smooth surfaces [25]. It was shown that for structures adhered to smooth surfaces, reduction in the atmospheric pressure from 1000 mbars to 1 mbars lead to a 20% reduction in the pull-off force. On rough surfaces the effect was reduced to 6%, hypothesized to be the result of improper sealing at the contact edge. Purtov et al. presented a study on similar sub-millimeter-scale structures which showed a reduction in pull-off force in the absence of suction of  $\sim 25\%$  [26].

While it is difficult to draw absolute conclusions from the preceding literature given differences in the details of the fabrication processes, substrates, and measurement systems, there is evidence that suction may influence the strength of attachment in micropatterned adhesives utilizing mushroom-shaped microstructures under certain conditions. Furthermore, these studies have suggested that the suction contribution may scale with the mushroom tip size [23,25,26]. In this work, we seek to investigate the role of suction in greater detail. We develop a model based upon linear elastic fracture mechanics to determine the strength of attachment of structures as a function of various system parameters, including the geometric and material properties, the adhesive strength of the interface, the ambient atmospheric pressure, and the initial interfacial defect size and trapped volume of air. This model is used to explain the results of experimental investigation of millimeter-scale elastomeric mushroom-shaped structures. Since the properties of these structures differ from others in the literature (larger length-scale, wider flanged tips), more general insights provided by the model are also explored.

Figure 1 is a schematic depiction of the system considered, encompassing both experimental and modeling efforts. The mushroom-shaped structure consists of a stalk and a flanged tip region, characterized by the geometric parameters shown in the

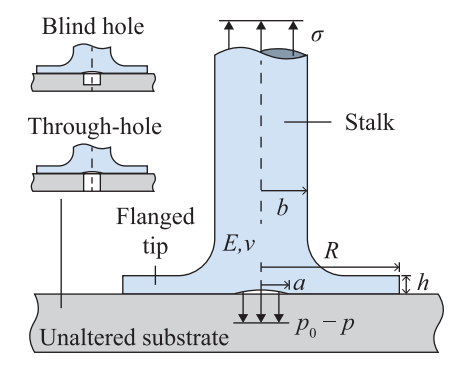


Fig. 1 Schematic of the adhesive structure, substrate, and loading configuration. The geometric parameters of the structure are shown, along with the properties of the component material. The tractions on free surfaces of the structure are also shown, namely, the applied stress,  $\sigma$ , and the net traction due to reduced pressure inside of the defect,  $p_0 - p$ .

figure. Detachment is primarily associated with the propagation of a defect from the contact center, also depicted in the figure. If air is trapped in the defect as it propagates, and if the time scale of the detachment process is faster than those of leakage flow through asperities at the interface or permeation through the structure, then reduced pressure will develop in the defect. As illustrated in the figure, this results in a net tensile traction exerted on the structure inside of the defect, increasing the resistance to further separation. Three substrate configurations are considered experimentally to assess the role of this suction effect on the attachment strength of the structure. In addition to an unaltered substrate, a sample with a through-hole is created. This is centered with respect to the stalk to eliminate the possibility of reduced pressure developing inside of the defect. Given that this hole could be viewed as a preexisting flaw in the contact, an additional control is considered with a blind hole of the same diameter and location.

### 2 Materials and Methods

**2.1 Fabrication of Structures.** The bio-inspired structures are generated by replica molding using 3D printed masters. The 3D geometries are produced in Solidworks (Dassault Systèmes, Vélizy-Villacoublay, France). Each mimic consists of a thin stalk of radius 1.5 mm that terminates in a larger disk of 6.0 mm radius that mimics the general features of mushroom-shaped fibrils (Supplemental Figure S1 available in the Supplementary Materials on the ASME Digital Collection). The fillet radius at the connection of the stalk and flanged tip was 5 mm, and the cap thickness was 0.5 mm at the outer edge. The top of the structure terminates in a thick cylindrical button to enable clamping and pulling in the tensile testing device. A second, smaller fillet was added at the top of the stalk where it meets the button to reduce stress concentrations and prevent failure at this junction. Each mold comprises four pieces (Supplemental Figure S2 available in the Supplementary Materials on the ASME Digital Collection): two identical halves that when fitted together create the main shape, as well as a top and bottom plate that seal and secure the structure. Each mold allows the formation of five identical structures for mechanical testing. Molds are printed with a Stratasys Objet30 Pro 3D (Stratasys, Eden Prairie, MN) printer using Rigur simulated polypropylene (RGD 450) print material and SUP 705 support material. All molds are printed with a glossy finish. The surface roughness of the molds is found to be highly dependent on the age of the print heads. To ensure that the surface roughness was kept constant across all conditions, the same molds were used to fabricate all samples. Surface roughness data are not available for the specific mold used to fabricate the samples tested for this paper. However, surface roughness measurements for other glossy surfaces on the same printer exhibited a root mean squared amplitude of 140 nm  $\pm$  55 nm (N = 3) when characterized using a DektakXT Stylus Profilometer (Bruker, Billerica, MA) with a scan length of 2500  $\mu$ m. After printing, each mold is cleaned to remove support material, first by hand with a razor blade, and then by blasting with water. Molds are then towel dried and outgassed for 6 h at a minimum temperature of 60 °C in a 1310 standard oven (VWR, Cornelius, OR). Outgassing the molds before use prevents the structures from sticking during the demolding process.

The adhesive structures are generated by injection of a thermally curable commercial polydimethylsiloxane (PDMS) elastomer (Sylgard 184, Dow Corning, Midland, MI) into the custom molds. PDMS was selected because it is well-characterized, its mechanical and interfacial properties enable significant sample deformation under modest loads, and bonding conditions that bias adhesive failure can be achieved [28]. Before injection, the PDMS is mixed by hand at a 10:1 weight ratio of base to crosslinking agent, per the manufacturer's instructions, and degassed for at least 5 min. The mixture is immediately injected using 5 ml syringes into the molds and cured for 2 h at 75 °C before being released from the molds.

**2.2 Substrate Preparation and Bonding of Structures.** Before attachment of the mushroom-shaped structures, each

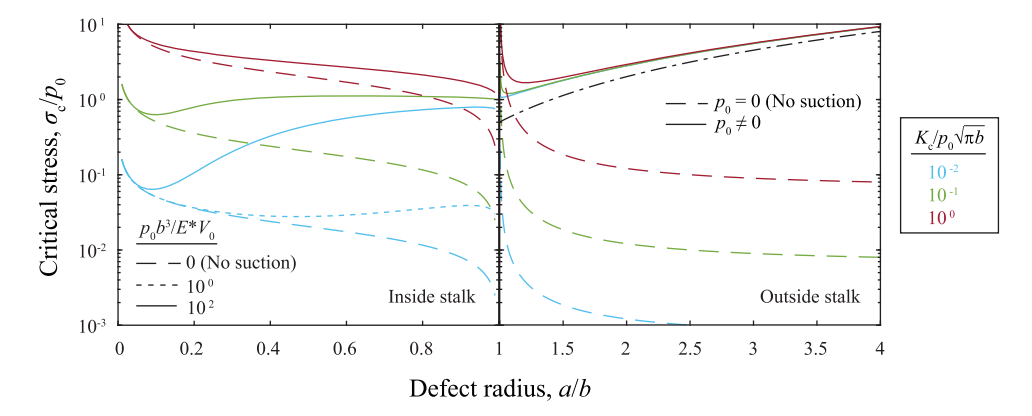


Fig. 2 Normalized critical stress,  $\sigma_c/p_0$ , versus normalized defect radius, a/b, for three values of the dimensionless interface toughness parameter,  $K_c/p_0\sqrt{\pi b}$ . The same results are shown without the effect of suction. Limiting behavior when the interfacial defect radius is inside (left) and outside (right) of the fibril stalk is shown. In the latter case, a single value of the normalized flange thickness, h/b = 0.1, is considered. The black dashed line (outside stalk) represents the limiting behavior of Eq. (25).

substrate (borosilicate microscope slides, 25 mm × 75 mm) is etched using a Speedy 100 laser cutter (Trotec, Marchtrenk, Austria) to create a circular alignment marker at its center. To decouple the effects of suction and adhesion under defect propagation, three substrate configurations are fabricated (Fig. 1). Both configurations with holes are created by drilling using a CNC mill (Sherline, Vista, CA) controlled with a microstepping controller (Flashcut CNC, Deerfield, IL). The diameter of each is 0.75 mm, with the blind hole drilled to a depth of 0.44 mm. The holes are centered with respect to the stalk. After the holes are drilled, the slides are cleaned with isopropanol to remove glass debris and other contaminants. Within 24 h of thermally curing the PDMS structures, they are adhered to the substrate. The bonding process involves treatment of the PDMS structures and the microscope slides for 10 min in an UV-Ozone cleaner (PSD-UV6, Novascan, Boone, IA) to remove organic contaminants. Immediately following the ozone treatment, each structure is placed directly on a microscope slide with sufficient contact pressure to remove trapped air bubbles and form the adhesive bond. All structures are then mechanically tested within 3 h of this bonding process.

**2.3 Mechanical Testing.** The synthetic structures are loaded to failure using a custom-built tensile tester with multi-camera imaging capabilities (Supplemental Figure S3 available in the Supplementary Materials on the ASME Digital Collection). A Lebow Load Cell (Model 3108–10, 10-lb capacity Honeywell Sensing & Control, Charlotte, NC) with custom amplifying electronics is connected to a computer via a USB-mediated data acquisition (DAQ) module (DT9804, Measurement Computing, Norton, MA). Command of the stepper motor (ES22B, Parker CompuMotor, Irwin, PA) via an indexer controller (ZETA 6104, Parker Compu-Motor, Irwin, PA), as well as acquisition of force and displacement data, is performed in LABVIEW (National Instruments, Austin, TX). The microscope slide and the adhered sample are placed on the stage and the center of the structure was aligned by eye to the center of the load cell (Supplemental Figure \$3 available in the Supplementary Materials on the ASME Digital Collection). The button at the free end of the sample is placed inside custom clamps and again centered by eye. The experiments are conducted under displacement control. The strain rate for all experiments presented is 0.004 s<sup>-1</sup>, which is calculated by dividing crosshead velocity (2.5 mm/min) by the stalk length.

The deformation of the structure is recorded during each tensile test using a Canon Rebel SL2 with a Canon 100 mm f/2.8 Macro USM fixed lens. This camera captures the structural deformation of the whole sample from a "front view," at a rate of 30 frames per second (fps). Defect growth rates are determined by measuring

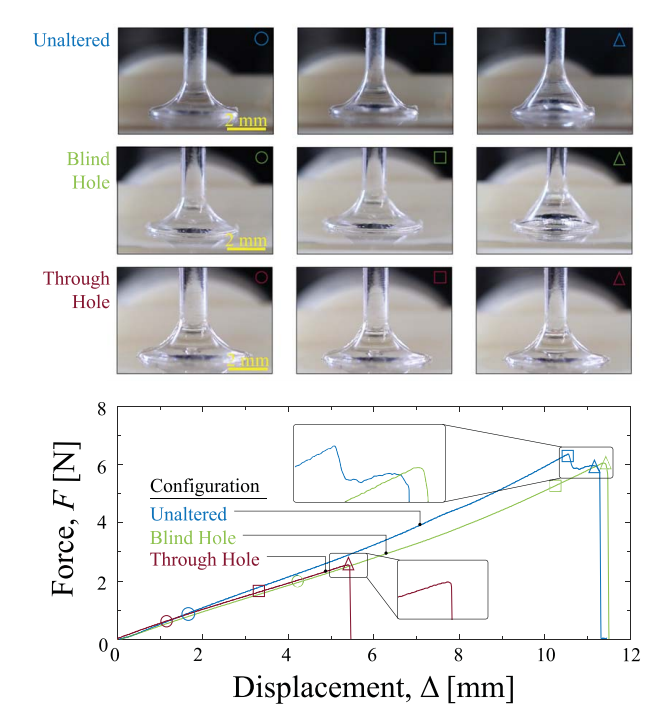


Fig. 3 Representative force–displacement trace for structures adhered to each substrate configuration. The markers indicate time points at which images of the structures (above) were captured. All curves are labeled according to the configuration.

the defect diameter in screenshots taken from these videos (Supplemental Figure S4 available in the Supplementary Materials on the ASME Digital Collection).

To enable statistically meaningful comparisons of the force-extension data collected with different samples and loading schemes, the distributions of forces and elongations at failure were compared using a pairwise Student's *t*-test implemented in MATLAB (Mathworks, Natick, MA).

# 3 Model

Returning to the schematic shown in Fig. 1, we consider the defect to be penny-shaped with radius a, located at the center of the contact. The stalk has radius b, and the flanged tip has radius R.

The thickness of the flanged tip is h. The fibril is subject to an applied tensile stress,  $\sigma$ . Prior to application of stress ( $\sigma$ =0), the defect is considered to have initial volume  $V_o$ . As the applied stress is increased, deformation and eventual propagation of the defect cause the volume inside, V, to increase. If air is trapped within the defect as this occurs, then the absolute pressure inside the defect, p, will be reduced. Assuming that the initial trapped volume of air is at ambient atmospheric pressure,  $p_0$ , then the ideal gas law for the air in the defect provides

$$p = p_0 \frac{V_0}{V} \tag{1}$$

The net effect on the structure will be a tensile traction of magnitude  $p_0-p$ , acting on the bottom surface of the tip over the cross-sectional area of the defect, as shown in Fig. 1. In general, as the volume in the defect increases, the absolute pressure will be reduced, and the magnitude of this tensile traction will increase. We seek to introduce a model based on linear elastic fracture mechanics to examine how this suction effect influences defect growth, in combination with the adhesive strength of the interface. The ultimate goal is to determine the maximum applied stress which can be supported by the structure prior to complete detachment.

3.1 Interfacial Defect Radius Inside of the Fibril Stalk. In the limit that the defect radius is smaller than that of the fibril stalk, a < b, the analysis can be performed by approximating the fibril as a straight sided cylinder of radius b. Under the assumption of a frictionless interface, linear elastic fracture mechanics provides the solution for the stress intensity factor at the outer perimeter of the defect when subject to a remote tensile stress and a uniform traction on the defect surface as [29]

$$K_{\rm I} = \frac{2}{\pi} (\sigma + p - p_0) \sqrt{\pi a} f\left(\frac{a}{b}\right) \tag{2}$$

where

$$f\left(\frac{a}{b}\right) = \frac{1 - \frac{1}{2}\frac{a}{b} + 0.148\left(\frac{a}{b}\right)^3}{\sqrt{1 - \frac{a}{b}}}\tag{3}$$

Invoking Eq. (1), the stress intensity factor can be rewritten in a dimensionless form as

$$\frac{K_{\rm I}}{p_0\sqrt{\pi b}} = \frac{2}{\pi} \left(\frac{\sigma}{p_0} + \frac{V_0}{V} - 1\right) \sqrt{\frac{a}{b}} f\left(\frac{a}{b}\right) \tag{4}$$

The volume of the defect is also given by linear elastic fracture mechanics as [29]

$$V = V_0 + \frac{8a^3}{3F^*}(\sigma + p - p_o)g\left(\frac{a}{b}\right)$$
 (5)

where

$$g\left(\frac{a}{b}\right) = \frac{1}{\left(\frac{a}{b}\right)^3} \left[ 1.260 \ln\left(\frac{1}{1 - \frac{a}{b}}\right) - 1.260 \left(\frac{a}{b}\right) - 0.630 \left(\frac{a}{b}\right)^2 + 0.580 \left(\frac{a}{b}\right)^3 - 0.315 \left(\frac{a}{b}\right)^4 - 0.102 \left(\frac{a}{b}\right)^5 + 0.063 \left(\frac{a}{b}\right)^6 + 0.093 \left(\frac{a}{b}\right)^7 - 0.0081 \left(\frac{a}{b}\right)^8 \right]$$

and  $E^*=E/(1-\nu^2)$ , where E is the Young's modulus and  $\nu$  the Poisson's ratio. Introducing Eq. (1) we obtain a quadratic equation

for the volume

$$\left(\frac{V}{V_0}\right)^2 - \left[1 + \frac{8}{3} \frac{p_0 b^3}{E^* V_0} \left(\frac{\sigma}{p_0} - 1\right) \left(\frac{a}{b}\right)^3 g\left(\frac{a}{b}\right)\right] \frac{V}{V_0}$$
$$-\frac{8}{3} \frac{p_0 b^3}{E^* V_0} \left(\frac{a}{b}\right)^3 g\left(\frac{a}{b}\right) = 0 \tag{7}$$

the solution of which is

$$\frac{V}{V_0} = \frac{1}{2} + \frac{4}{3} \frac{p_0 b^3}{E^* V_0} \left(\frac{\sigma}{p_0} - 1\right) \left(\frac{a}{b}\right)^3 g\left(\frac{a}{b}\right) + \frac{1}{2}$$

$$\times \sqrt{\left[1 + \frac{8}{3} \frac{p_0 b^3}{E^* V_0} \left(\frac{\sigma}{p_0} - 1\right) \left(\frac{a}{b}\right)^3 g\left(\frac{a}{b}\right)\right]^2 + \frac{32}{3} \frac{p_0 b^3}{E^* V_0} \left(\frac{a}{b}\right)^3 g\left(\frac{a}{b}\right)}$$
(8)

Defect growth occurs when the stress intensity factor reaches a critical value, characteristic of the strength of the adhesive bond at the interface,  $K_1 = K_c = \sqrt{2E^*W}$ , where  $K_c$  is termed the interfacial toughness and W is the work of adhesion. In combination with Eqs. (4) and (8), this condition can be used to solve for the corresponding critical stress  $\sigma = \sigma_c$ . For the results presented in Sec. 4.1, this was achieved numerically in MATLAB (Mathworks, Natick, MA).

A closed-form solution for the critical stress is possible for the condition in which air is not sealed within the defect, or where the structure is placed in a vacuum environment. We refer to this situation as "No Suction" (NS). In this case  $p_0 = 0$ , and

$$\sigma_c^{\rm NS} = \frac{\pi}{2f\left(\frac{a}{b}\right)} \frac{K_c}{\sqrt{\pi a}} \tag{9}$$

or in terms of equivalent dimensionless parameters to those in Eq. (4), as

$$\left(\frac{\sigma_c}{p_0}\right)_{\rm NS} = \frac{\pi}{2f\left(\frac{a}{b}\right)} \sqrt{\frac{b}{a}} \left(\frac{K_c}{p_0 \sqrt{\pi b}}\right) \tag{10}$$

**3.2** Interfacial Defect Radius Outside of the Fibril Stalk. In this case, we assume that the mushroom flange is thin  $(h \ll R)$  and wide  $(R \gg b)$ , and thus its deformation can be treated by Kirchhoff-Love plate theory. The deflection is therefore given by solution of the biharmonic equation for an axisymmetric system [30]. We establish a radial coordinate r, defined from the center of the contact. The boundary conditions are determined under the assumption that in comparison with the flange, the fibril stalk can be considered rigid. Consequently, the rotation of the section where the flange meets the stalk, and at the perimeter of the defect is assumed to be zero. The solution for the deflection due to the remote load, based on an applied shear force where the flange meets the stalk, is

$$w(r) = \frac{3\sigma b^4}{4E^*h^3 \left[ \left(\frac{a}{b}\right)^2 - 1 \right] \left[ \left(\frac{a}{b}\right)^2 - 1 \right] \left[ \left(\frac{a}{b}\right)^2 - \left(\frac{r}{b}\right)^2 \right]$$

$$+ 2\left(\frac{a}{b}\right)^2 \left(\frac{r}{b}\right)^2 \ln\left(\frac{r}{a}\right) - 2\left(\frac{r}{b}\right)^2 \ln\left(\frac{r}{b}\right)$$

$$+ 2\left(\frac{a}{b}\right)^2 \ln\left(\frac{a}{b}\right) + 4\left(\frac{a}{b}\right)^2 \ln\left(\frac{a}{b}\right) \ln\left(\frac{r}{a}\right)$$

$$(11)$$

in the region  $b \le r \le a$  and

$$w(b) = \frac{3\sigma b^4}{4E^*h^3 \left[ \left(\frac{a}{b}\right)^2 - 1 \right]} \left\{ \left[ \left(\frac{a}{b}\right)^2 - 1 \right]^2 - 4\left(\frac{a}{b}\right)^2 \ln\left(\frac{a}{b}\right) \ln\left(\frac{a}{b}\right) \right\}$$
(12)

in the region  $0 \le r \le b$ . In treating the pressure contribution, it is assumed that the volume in the defect is very large as compared with that which was initially trapped. As a result, we assume vacuum conditions have developed in the defect (p=0). The tensile traction applied to the bottom surface of the structure inside of the defect is therefore  $p_0$  (Fig. 1). This enters the plate theory formulation as an applied shear force where the flange meets the stalk (associated with the tensile traction under the stalk) and a uniform distributed load on the region outside of the stalk to the perimeter of the defect. Together, these lead to the solution for deflection due to the tensile traction inside of the defect

$$w(r) = -\frac{3p_0b^4}{16E^*h^3} \left\{ \left(\frac{r}{b}\right)^4 - \left(\frac{a}{b}\right)^4 + 2\left[\left(\frac{a}{b}\right)^2 + 1\right] \right.$$
$$\times \left[ \left(\frac{a}{b}\right)^2 - \left(\frac{r}{b}\right)^2 \right] + 4\left(\frac{a}{b}\right)^2 \ln\left(\frac{r}{a}\right) \right\}$$
(13)

in the region  $b \le r \le a$  and

$$w(b) = -\frac{3p_0b^4}{16E^*h^3} \left[ \left(\frac{a}{b}\right)^4 - 1 - 4\left(\frac{a}{b}\right)^2 \ln\left(\frac{a}{b}\right) \right]$$
 (14)

in the region  $0 \le r \le b$ . To compute the strain energy,  $U(\sigma, p_0)$  we first compute the result for  $\sigma$  alone and obtain

$$U(\sigma,0) = \frac{3\sigma^2\pi b^6}{8E^*h^3\left[\left(\frac{a}{b}\right)^2 - 1\right]} \left\{ \left[\left(\frac{a}{b}\right)^2 - 1\right]^2 - 4\left(\frac{a}{b}\right)^2 \ln\left(\frac{a}{b}\right) \ln\left(\frac{a}{b}\right) \right\}$$

Maintaining  $\sigma$  as fixed, the pressure  $p_0$  is increased from zero. The increment of additional strain energy is given by

$$dU = (\sigma - p_0)\pi b^2$$

$$\times \left\{ -\frac{3dp_0b^4}{16E^*h^3} \left[ \left( \frac{a}{b} \right)^4 - 1 - 4\left( \frac{a}{b} \right)^2 \ln\left( \frac{a}{b} \right) \right] \right\}$$

$$+ \int_b^a \left( -\frac{3dp_0b^4}{16E^*h^3} \left\{ \left( \frac{r}{b} \right)^4 - \left( \frac{a}{b} \right)^4 + 2\left[ \left( \frac{a}{b} \right)^2 + 1 \right] \right.$$

$$\times \left[ \left( \frac{a}{b} \right)^2 - \left( \frac{r}{b} \right)^2 \right] + 4\left( \frac{a}{b} \right)^2 \ln\left( \frac{r}{a} \right) \right\} (-p_o) 2\pi r dr$$
(16)

where the first term is associated with the region under the stalk, and the second term is associated with the region outside of the stalk to the perimeter of the defect. Integration over the outer region yields

$$dU = -\frac{3\pi b^6}{16E^*h^3} \left[ \left( \frac{a}{b} \right)^4 - 1 - 4 \left( \frac{a}{b} \right)^2 \ln \left( \frac{a}{b} \right) \right] \sigma dp_0$$

$$+ \frac{\pi b^6}{16E^*h^3} \left[ \left( \frac{a}{b} \right)^2 - 1 \right]^3 p_0 dp_0$$
(17)

Upon integration of the load parameters, this leads to

$$U(\sigma, p_0; a) = \frac{3\sigma^2 \pi b^6}{8E^* h^3} \left[ \left( \frac{a}{b} \right)^2 - 1 - \frac{4\left( \frac{a}{b} \right)^2 \ln\left( \frac{a}{b} \right) \ln\left( \frac{a}{b} \right)}{\left( \frac{a}{b} \right)^2 - 1} \right] - \frac{3\sigma p_0 \pi b^6}{16E^* h^3} \left[ \left( \frac{a}{b} \right)^4 - 1 - 4\left( \frac{a}{b} \right)^2 \ln\left( \frac{a}{b} \right) \right] + \frac{p_0^2 \pi b^6}{32E^* h^3} \left[ \left( \frac{a}{b} \right)^2 - 1 \right]^3$$
(18)

The energy release rate is given by

$$\mathcal{G} = \frac{1}{2\pi a} \frac{\partial U(\sigma, p_0; a)}{\partial a}$$
 (19)

which, in combination with the result of (18), leads to

$$\mathcal{G} = \frac{3p_0^2b^4}{8E^*h^3} \left\{ \frac{\sigma}{p_0} \left[ 1 - \frac{2\ln(\frac{a}{b})}{\left(\frac{a}{b}\right)^2 - 1} \right] - \frac{1}{2} \left[ \left(\frac{a}{b}\right)^2 - 1 \right] \right\}^2$$
 (20)

Once again, defect growth is known to occur when the energy release rate attains a critical value characteristic of the strength of the adhesive bond at the interface, which in this case is the work of adhesion,  $\mathcal{G} = W = K_c^2/2E^*$ . In combination with Eq. (20), this condition can be used to solve for the corresponding critical stress  $\sigma = \sigma_c$  as

(13) 
$$\frac{\sigma_{c}}{p_{0}} = \frac{\left(\frac{a}{b}\right)^{2} - 1}{\left(\frac{a}{b}\right)^{2} - 1 - 2\ln\left(\frac{a}{b}\right)} \left\{ \frac{1}{2} \left[ \left(\frac{a}{b}\right)^{2} - 1 \right] + \left(\frac{4\pi}{3}\right)^{1/2} \left(\frac{h}{b}\right)^{3/2} \frac{K_{c}}{p_{0}\sqrt{\pi b}} \right\}$$

In the situation in which air is not trapped within the defect, or equivalently the junction is formed in conditions of zero atmospheric pressure  $(p_0 = 0)$ , the critical stress will be

$$\sigma_c^{\text{NS}} = \frac{\left(\frac{a}{b}\right)^2 - 1}{\left(\frac{a}{b}\right)^2 - 1 - 2\ln\left(\frac{a}{b}\right)} \left(\frac{4\pi}{3}\right)^{1/2} \left(\frac{h}{b}\right)^{3/2} \frac{K_c}{\sqrt{\pi b}}$$
(22)

This can be stated in an equivalent dimensionless form to Eq. (21), as

$$\left(\frac{\sigma_c}{p_0}\right)_{NS} = \frac{\left(\frac{a}{b}\right)^2 - 1}{\left(\frac{a}{b}\right)^2 - 1 - 2\ln\left(\frac{a}{b}\right)} \left(\frac{4\pi}{3}\right)^{1/2} \left(\frac{h}{b}\right)^{3/2} \frac{K_c}{p_0\sqrt{\pi b}} \tag{23}$$

# 4 Results and Discussion

**4.1 Model.** Figure 2 shows the normalized critical stress,  $\sigma_c/p_0$ , required to drive defect growth, as a function of the normalized defect radius, a/b, in both limits presented in Sec. 3. Three values of the dimensionless interface toughness parameter,  $K_c/p_0\sqrt{\pi b}$ , are considered. In the limit in which the defect is inside of the fibril stalk, three values of the dimensionless pressure parameter,  $p_0b^3/E^*V_0$  are considered (although the intermediate value is omitted for higher toughness to preserve clarity of the plot). In the limit that the defect is outside of the fibril stalk, we show the results with suction  $(p_0 \neq 0, \text{ Eq. (21)})$  and without suction  $(p_0 = 0, \text{ Eq. (23)})$ , and consider a single value of the normalized flange thickness, h/b = 0.1.

The normalized critical stress is seen to increase with the pressure parameter,  $p_0b^3/E^*V_0$ . This is a result of an enhancement of the suction effect introduced in Sec. 3. The tensile traction on the bottom of the structure inside of the defect (Fig. 1), which results when the volume of air trapped within increases and the pressure is reduced, acts to pull the defect closed. This allows for a higher magnitude of applied stress to be supported without defect growth. A larger tensile traction develops when the ambient atmospheric pressure,  $p_0$  (outside of the defect) is high or the initial trapped volume in the defect,  $V_0$ , is small. Larger structures (increased b) and more compliant materials (reduced  $E^*$ ) allow for greater increases in defect volume, greater reduction of the pressure inside the defect, and thus also a larger tensile traction.

Considering the behavior when the defect is inside of the stalk in greater detail, we observe a monotonic decay in the normalized critical stress with increasing defect size when interface toughness is high (e.g., for  $K_c/p_0\sqrt{\pi b}=1$ ). This indicates unstable defect propagation. The dominant effect during defect growth is an increase in the stress intensity at the defect perimeter associated with the remote

applied stress. The high toughness renders the stresses required for defect growth higher than can be supported by tensile tractions inside of the defect due to the pressure difference alone. Consequently the critical stress is found to exceed the ambient pressure,  $\sigma_c/p_0 > 1$ , across the relevant range of defect radius. It is observed that the normalized critical stress is reduced as the toughness of the interface is reduced. A regime of stable defect growth may emerge, evidenced by an increase in the normalized critical stress defect radius (e.g., for  $K_c/p_0\sqrt{\pi b} = 0.01$  $K_c/p_0\sqrt{\pi b} = 0.1$ ). In this case, the dominant effect of defect growth is reduction of pressure inside of the defect. If the value of the parameter  $p_0b^3/E^*V_0$  is sufficiently high, the results asymptotically approach a critical stress equal to the ambient pressure,  $\sigma_c/p_0 \rightarrow 1$ , as the defect approaches the edge of the stalk. Under these conditions, the absolute pressure inside of the defect is negligible (p=0). Consequently, the tensile traction on the bottom surface of the structure due to the suction effect is maximized, being equal to the ambient atmospheric pressure,  $p_0$ . As the defect approaches the edge of the stalk,  $a/b \rightarrow 1$ , the applied stress is almost entirely supported by this tensile traction on the bottom of the structure.

At the point of transition between limiting behaviors,  $a/b \rightarrow 1$ , the prediction of the critical stress from plate theory approaches infinity. This unphysical result is a consequence of the absence of strain energy in the flange in this limit, as per Eq. (15). In reality, as the defect passes through this region, the stress will exhibit a smooth transition between the limits provided that the pressure in the defect, p, is sufficiently close to zero (as is assumed in the plate theory formulation). If this is not the case (e.g., pale blue small dashed line), then the actual critical stress will be lower than the prediction of plate theory until the defect has grown sufficiently and the pressure inside is effectively zero.

Considering the behavior when the defect is outside of the stalk, we observe that in the absence of suction the critical stress continues to decrease monotonically. The defect propagation remains unstable, as it was inside of the stalk in this case. Consequently, the maximum value of applied stress (thus the strength of attachment of the structure in load control) will be attained prior to defect propagation, and thus controlled by the initial defect size.

In the presence of suction, the dominant effect when the defect is outside of the stalk is an increase in the critical stress with the defect radius. This behavior is simply the result of the recruitment of more area over which the tensile traction on the bottom of the structure, due to the suction effect, may act. It is observed that the behavior, with increasing defect radius, approaches a limit independent of the toughness of the interface. It is therefore illustrative to consider the critical stress when interfacial bonding is negligible and suction dominates. When the toughness is zero, Eq. (21) yields

$$\left(\frac{\sigma_c}{p_0}\right)_{K_c=0} = \frac{1}{2} \frac{\left[\left(\frac{a}{b}\right)^2 - 1\right]^2}{\left(\frac{a}{b}\right)^2 - 1 - 2\ln\left(\frac{a}{b}\right)}$$
(24)

In the limit that the defect is large,  $a \gg b$ , we reach

$$\frac{\sigma_c}{p_0} = \frac{1}{2} \left(\frac{a}{b}\right)^2 \tag{25}$$

This result is shown as a black dashed line in Fig. 2. This limiting case is quite significant, as it differs by a factor of 1/2 from the critical stress that is calculated by a simple balance of forces associated with the applied stress and the tensile traction on the bottom of the structure due to suction. Such an approach to approximate the suction contribution is suggested in Ref. [15] and is revealed here to be an overestimate of the effect by 100%. Plate theory reveals

the source of this discrepancy. When the shear force (per unit length) on the cross section around the perimeter of the defect (i.e., at r=a) is considered, we obtain

$$Q = \frac{\sigma b^2}{2a} - \frac{1}{2}p_0 a \tag{26}$$

When the critical stress is given by Eq. (25), the shear force is therefore

$$Q = -\frac{1}{4}p_0a\tag{27}$$

This negative shear implies that the interface supports compressive tractions outside of the defect. This compression of the flanged tip against the substrate supports half of the total load generated by the tensile tractions due to the suction effect, thus lowering the critical stress.

In summary, since the critical stress in the presence of suction is nonmonotonic, the width of the tip will dictate whether the maximum value of critical stress is attained with the defect inside or outside of the stalk, and thus whether the presence of the flanged tip is of significance to the strength of the structure. If the tip is not wide relative to the stalk, then the maximum value of the critical stress is attained when the defect is under the stalk. By the time it reaches the flange, its propagation will be unstable. However, if the tip is wide, eventually the critical stress will be larger than that which was observed under the stalk. The maximum stress will be attained as the defect approaches the edge of the tip, thus the strength will be controlled by its width. Under these conditions, it is most advantageous to make the tip as wide as possible without violation of its structural integrity or other manufacturing constraints.

**4.2 Comparison With Experiment.** Figure 3 shows representative force-extension curves for the different configurations described in Sec. 2.2. In all cases, we observe an increase in force with increasing extension up until the onset of detachment, consistent with elastic deformation of the stalk. Table 1 shows the maximum force  $F_{\text{max}}$  and extension to failure  $\Delta_{\text{max}}$ . In the SI, box plots for these results are also provided (Supplemental Figure S5 available in the Supplementary Materials on the ASME Digital Collection). Significance is assessed using pairwise Student's t-tests for the various slide configurations, p < 0.05. A full accounting of the results of the statistical analysis of these data are provided in the SI (Supplemental Table S1 available in the Supplementary Materials on the ASME Digital Collection). The maximum force and extension to failure are largest for structures adhered to unaltered glass slides, or slides with a blind hole. The difference in these two cases is not statistically significant, suggesting that the presence of the hole alone does not control the strength of attachment. By contrast, structures adhered to glass slides with a through-hole, designed to prevent the trapping of air within the defect, exhibited a significant drop in the maximum force. The reduction, as compared with the other two cases, is on the order

Table 1 Average maximum force (and associated standard deviation) and average maximum elongation (and associated standard deviation) measured experimentally

Substrate configuration	Average maximum force $F_{\text{max}}$ (N)	Average maximum elongation $\Delta_{max}$ (mm)
Unaltered	$6.88 \pm 1.56$	10.74 ± 1.16
Blind hole	$5.94 \pm 1.76$	$10.11 \pm 1.94$
Through-hole	$2.50 \pm 0.42$	$4.73 \pm 0.78$

Note: The number of experiments was between 10 and 14 per substrate configuration.

<sup>&</sup>lt;sup>4</sup>We note that Carbone *et al.* [14] erroneously use this artificial divergence to claim that a fibril can have infinite adhesion strength when the defect radius coincides with that of the stalk.

of 60%. Alternatively, suction can be viewed as providing an enhancement of the maximum force on the order of  $\sim$ 150%.

In order to compare the results with the model presented, it is first necessary to consider the nature of defect propagation and the defect size at which the maximum load is observed. Simultaneous imaging of the detachment dynamics during loading is employed, as shown in Videos 1–2 in the Supplementary Materials on the ASME Digital Collection. Figure 3 also shows snapshot images of the loaded structures at various stages of structure–substrate separation.

In the cases of an anticipated suction contribution, for the unaltered substrate (Fig. 3, blue images and Video 1 in the Supplementary Materials on the ASME Digital Collection) and blind hole substrate (Fig. 3, green images), a defect at the center of the contact begins to propagate at a critical load and grows stably. Specifically, for the unaltered substrate, initiation occurs at a load of ~3 N. The defect is then observed to grow at a constant rate of  $0.16 \pm 0.02$  mm/s, passing the edge where the stalk meets the flange; we denote this as Regime 1. At a load of ~5 N, when the defect extends outside of the stalk, the defect growth rate slows considerably to a value of  $0.051 \pm 0.003$  mm/s; we denote this as Regime 2. When load reaches ~6 N (i.e., at the point of approximately maximal load) the defect grows rapidly toward the edge of the tip. As the defect reaches the edge, a cupping effect is observed consistent with flange deformation. In this regime, it is not possible to accurately measure the defect growth rate. Flange deformation is followed by the final detachment of the structure from the substrate. Results for the defect growth rate obtained from measurements of three additional structures are included in the Supplementary Materials (Supplemental Table S2 available in the Supplementary Materials on the ASME Digital Collection).

The slowing of the defect growth in the flange region is evidence of an increase in the critical stress, which was predicted in the preceding model when suction was present and the defect was outside of the stalk. This suggests that the overall strength will be controlled by the tip radius, R. Experimental observations of the radius of the defect at the point of maximum load,  $a_{\text{max}}$ , suggest that the ratio  $a_{\text{max}}/b > 3$ . This is approaching the tip-stalk ratio, R/b = 4. Further evidence of the critical role played by the radius of the tip is the observation that the experimental results appear independent of the initial defect size. There is minimal difference in the maximum force supported by the unaltered substrate (with no perceptible initial defect) and the blind hole substrate (with the hole representing a well-characterized initial defect size).

When the defect is far outside of the stalk and a suction effect is present, the preceding model suggests that the strength is approximately independent of the toughness of the interface and is thus well approximated by Eq. (25). Using the tip radius as an estimate of the defect size at maximum load,  $a_{\text{max}}/b = 4$ , in combination with the result of Eq. (25) we obtain an estimate of the strength of the attachment  $\sigma_{\rm max} \sim 900 \, \rm kPa$  or  $F_{\rm max} \sim 6.4 \, \rm N$ . This is in excellent agreement with the experimental observations and suggests that the strength is indeed controlled by the width of the flange relative to the stalk. It should be emphasized that this is the maximum value of the applied stress as defined in Fig. 1 and utilized in the model described in Sec. 3, which implicitly assumes normalization of the maximum applied force with respect to the cross-sectional area of the stalk. If instead the maximum applied force is normalized with respect to the projected area of the contact at the tip, then we obtain a strength of attachment of ~50 kPa.

In the case of the through-hole substrate, without the possibility of a suction contribution, different defect propagation behavior is observed (Fig. 3, red images and Video 2 in the Supplementary Materials on the ASME Digital Collection). A center defect is observed to start growing at a load of  $\sim 2.5$  N. Unsurprisingly, this is similar to the critical load for defect growth initiation in cases where a suction effect is possible, as suction cannot play a role until significant defect growth occurs. Unlike the other cases, once the defect begins to grow it propagates rapidly and the structure detaches completely (without arrest in the flange region). This is also consistent with the model presented, which predicts a

monotonic reduction in the critical stress (and thus unstable propagation) in the absence of suction.

**4.3 Comparison With Existing Literature.** The suction effect observed in the current study is considerably larger than in the existing literature (60% versus <25% [22–27]). There are two primary differences in the structures studied here. The first is the overall scale, being on the order of millimeters as compared with sub-millimeter [25,26] or micron [22–24,27]. The second is that the width of the flanged tip is considerably larger relative to the stalk than in previous studies (tip-stalk ratio of 4 versus <2 [22–27]). The model presented has revealed that the strength of attachment of the structures studied here is dominated by the tip-stalk ratio, via Eq. (25), hence it is the latter of the two differences which is primarily responsible for the difference observed.

The role played by the overall scale of the structures, while secondary here, may be more significant when the tip-stalk ratio is small. In this case the model presented predicts the strength will be controlled by behavior of the defect when it is inside of the stalk radius. In this regime, increases in the parameter  $p_0b^3/E^*V_0$  were seen to correspond to an increase in the suction effect. Fibrils with larger stalk radius, b, accommodate a greater volume change in the defect at an equivalent applied stress, thus a greater reduction in pressure within the defect. This is in agreement with general trends observed in the literature for small tip-stalk ratios [22–27], but detailed conclusions about this scaling will require examination of suction while systematically varying structure size.

### 5 Conclusions

New insights are presented on the contribution of suction to the attachment strength of mushroom-shaped structures. The critical stress required to drive defect propagation in the presence of trapped air at the interface is obtained as a function of the geometric, material, and interfacial properties of the system. A nonmonotonic critical stress in the presence of suction is evidenced in the model and confirmed in experiment by observation of arrest as the defect reaches the flange region. In experiment the reduction in strength in the absence of a suction effect is shown to be  $\sim 60\%$ , significantly higher than observed in previous studies which have showed effects <25%. The model presented shows this is primarily the result of the larger width of the flanged tip relative to the stalk. The larger overall length-scale of the structures may play a secondary role, associated with a tendency for larger volume change and thus lower pressure in the defect. An asymptotic result for the critical stress in the limit that the defect is far outside of the stalk reveals a regime independent of the toughness of the interface, in which the strength is lower by a factor of 1/2 than predicted by the balance of remote applied stress and net pressure inside of the defect. This is found to be the result of compressive tractions on the flange outside of the defect, which crucially have not been considered in the literature when approximating the effect of suction.

### Acknowledgment

This work was supported by the MRSEC Program of the National Science Foundation (NSF) under Award No. DMR 1720256 (IRG-3). Additionally, M. A. acknowledges support of the NSF California LSAMP Bridge to the Doctorate Fellowship under Grant No. HRD-1701365. D. B. acknowledges support of the Future Leaders in Advanced Materials NSF REU program under Award No. DMR 1460656. The authors acknowledge the use of the Microfluidics Laboratory within the California NanoSystems Institute, supported by the University of California, Santa Barbara and the University of California, Office of the President, as well as the Mechanical Test Laboratory of the UCSB Mechanical Engineering Department. The authors thank Younghoon Kwon for providing data on roughness of 3D printed surfaces.

### Conflict of Interest

There are no conflicts of interest.

### **Data Availability Statement**

The datasets generated and supporting the findings of this article are obtainable from the corresponding author upon reasonable request. The authors attest that all data for this study are included in the paper. Data provided by a third party listed in Acknowledgment.

### References

- [1] Desmond, K. W., Zacchia, N. A., Waite, J. H., and Valentine, M. T., 2015, "Dynamics of Mussel Plaque Detachment," Soft Matter, 11(34), pp. 6832-6839.
- [2] Autumn, K., and Peattie, A. M., 2002, "Mechanisms of Adhesion in Geckos," Integr. Comp. Biol., 42(6), pp. 1081–1090.
- [3] Gorb, S. N., and Varenberg, M., 2007, "Mushroom-Shaped Geometry of Contact Elements in Biological Adhesive Systems," J. Adhesion Sci. Technol., 21(12–13), pp. 1175-1183.
- [4] Autumn, K., Sitti, M., Liang, Y. A., Peattie, A. M., Hansen, W. R., Sponberg, S., Kenny, T. W., Fearing, R., Israelachvili, J. N., and Full, R. J., 2002, "Evidence for van Der Waals Adhesion in Gecko Setae," PNAS, 99(19), pp. 12252-12256.
- [5] Waite, J. H., 2017, "Mussel Adhesion—Essential Footwork," J. Exp. Biol., 220(4), pp. 517-530.
- [6] Autumn, K., Niewiarowski, P. H., and Puthoff, J. B., 2014, "Gecko Adhesion as a Model System for Integrative Biology, Interdisciplinary Science, and Bioinspired Engineering," Annu. Rev. of Eco., Evo., Sys., **45**(1), pp. 445–470. [7] Spuskanyuk, A. V., McMeeking, R. M., Deshpande, V. S., and Arzt, E., 2008,
- The Effect of Shape on the Adhesion of Fibrillar Surfaces," Acta Biomater., 4(6), pp. 1669-1676.
- [8] del Campo, A., Greiner, C., and Arzt, E., 2007, "Contact Shape Controls Adhesion of Bioinspired Fibrillar Surfaces," Langmuir, 23(20), pp. 10235–10243.
- [9] Heepe, L., and Gorb, S. N., 2014, "Biologically Inspired Mushroom-Shaped Adhesive Microstructures," Annu. Rev. Mater. Res., 44(1), pp. 173-203.
- [10] Li, Y., Krahn, J., and Menon, C., 2016, "Bioinspired Dry Adhesive Materials and Their Application in Robotics: A Review," J. Bionic Eng., 13(2), pp. 181–199.
- [11] Hensel, R., Moh, K., and Arzt, E., 2018, "Engineering Micropatterned Dry Adhesives: From Contact Theory to Handling Applications," Adv. Funct. Mater., 28(28), p. 1800865.
- [12] Khaderi, S. N., Fleck, N. A., Arzt, E., and McMeeking, R. M., 2015, "Detachment of an Adhered Micropillar From a Dissimilar Substrate," J. Mech. Phys. Solids, 75, pp. 159-183.
- [13] Balijepalli, R. G., Begley, M. R., Fleck, N. A., McMeeking, R. M., and Arzt, E., 2016, "Numerical Simulation of the Edge Stress Singularity and the Adhesion

- Strength for Compliant Mushroom Fibrils Adhered to Rigid Substrates," Int. J. Solids Struct., 85-86, pp. 160-171.
- [14] Carbone, G., Pierro, E., and Gorb, S. N., 2011, "Origin of the Superior Adhesive Performance of Mushroom-Shaped Microstructured Surfaces," Soft Matter, 7(12), pp. 5545-5552.
- [15] Afferrante, L., and Carbone, G., 2013, "The Mechanisms of Detachment of Mushroom-Shaped Micro-Pillars: From Defect Propagation to Membrane Peeling," Macromol. J. Macro. React. Eng., 7(11), pp. 609-615.
- [16] Minsky, H. K., and Turner, K. T., 2015, "Achieving Enhanced and Tunable Adhesion via Composite Posts," Appl. Phys. Lett., 106(20), p. 201604.
  [17] Minsky, H. K., and Turner, K. T., 2017, "Composite Microposts With High Dry
- Adhesion Strength," ACS Appl. Mater. Interfaces, 9(21), pp. 18322–18327.
- [18] Fischer, S. C. L., Arzt, E., and Hensel, R., 2017, "Composite Pillars With a Tunable Interface for Adhesion to Rough Substrates," ACS Appl. Mater. Interfaces, 9(1), pp. 1036–1044.
- [19] Bae, W. G., Kim, D., Kwak, M. K., Ha, L., Kang, S. M., and Suh, K. Y., 2013, "Enhanced Skin Adhesive Patch With Modulus-Tunable Composite Micropillars," Adv. Healthcare Mater., 2(1), pp. 109-113.
- [20] Fischer, S. C. L., Groß, K., Abad, O. T., Becker, M. M., Park, E., Hensel, R., and Arzt, E., 2017, "Funnel-Shaped Microstructures for Strong Reversible Adhesion," Adv. Mater. Interfaces, 4(20), p. 1700292.
- [21] Wang, Y., Kang, V., Arzt, E., Federle, W., and Hensel, R., 2019, "Strong Wet and Dry Adhesion by Cupped Microstructures," ACS Appl. Mater. Interfaces, 11(29), pp. 26483-26490.
- [22] Henrey, M., Díaz Téllez, J. P., Wormnes, K., Pambaguian, L., and Menon, C., 2013, "Towards the Use of Mushroom-Capped Dry Adhesives in Outer Space: Effects of Low Pressure and Temperature on Adhesion Strength," Aerospace Sci. Technol., 29(1), pp. 185–190.
- [23] Sameoto, D., Sharif, H., and Menon, C., 2012, "Investigation of Low-Pressure Adhesion Performance of Mushroom Shaped Biomimetic Dry Adhesives," J. Adhes. Sci. Technol., 26(23), pp. 2641-2652.
- [24] Heepe, L., Varenberg, M., Itovich, Y., and Gorb, S. N., 2011, "Suction Component in Adhesion of Mushroom-Shaped Microstructure," J. Royal Soci. Interface, 8(57), pp. 585-589.
- [25] Tinnemann, V., Hernández, L., Fischer, S. C. L., Arzt, E., Bennewitz, R., and Hensel, R., 2019, "In Situ Observation Reveals Local Detachment Mechanisms and Suction Effects in Micropatterned Adhesives," Adv. Funct. Mater., 29(14),
- [26] Purtov, J., Frensemeier, M., and Kroner, E., 2015, "Switchable Adhesion in Vacuum Using Bio-Inspired Dry Adhesives," ACS Appl. Mater. Interfaces, 7(43), pp. 24127-24135.
- [27] Davies, J., Haq, S., Hawke, T., and Sargent, J. P., 2009, "A Practical Approach to the Development of a Synthetic Gecko Tape," Int. J. Adhes. Adhes., 29(4), pp. 380–390.
- [28] Kim, T. K., Kim, J. K., and Jeong, O. C., 2011, "Measurement of Nonlinear Mechanical Properties of PDMS Elastomer," Microelectron. Eng., 88(8), pp. 1982-1985.
- [29] Tada, H., Paris, P. C., and Irwin, G. R., 2000, The Stress Analysis of Cracks Handbook, 3rd ed., ASME, NY,
- Timoshenko, S., and Woinowsky-Krieger, S., 1959, Theory of Plates and Shells, McGraw-Hill, New York.